

1 **Two-dimensional prognostic experiments for fast-flowing ice streams**
2 **from the Academy of Sciences Ice Cap**

3

4 **Y.V. Konovalov, O.V. Nagornov**

5

6 *Mathematical Department, National Research Nuclear University MEPhI (Moscow Engineering*
7 *Physics Institute), Kashirskoe shosse, 31, 115409, Moscow, Russian Federation*

8

9 Correspondence to: Y.V. Konovalov (yu-v-k@yandex.ru)

10

11 **Abstract**

12

13 The prognostic experiments for fast-flowing ice streams on the southern side of the Academy of
14 Sciences Ice Cap in the Komsomolets Island, Severnaya Zemlya archipelago, are implemented in
15 this study. These experiments are based on inversions of basal friction coefficients using a two-
16 dimensional flow-line thermo-coupled model and the Tikhonov's regularization method. The
17 modeled ice temperature distributions in the cross-sections were obtained using the ice surface
18 temperature histories that were inverted previously from the borehole temperature profile derived
19 at **the summit** of the Academy of Sciences Ice Cap **and employing elevational gradient of ice**
20 **surface temperature changes, which is equal to about $6.5 \text{ }^{\circ}\text{C km}^{-1}$** . Input data included InSAR ice
21 surface velocities, ice surface elevations, and ice thicknesses obtained from airborne
22 measurements and the surface mass balance, were adopted from **previous** investigations for the
23 implementation of both the forward and inverse problems. The prognostic experiments reveal that
24 both ice mass and ice stream extents decline for the reference time-independent surface mass

25 balance. Specifically, the grounding line retreats (a) along the B–B' flow line from ~40 km to ~30
26 km (the distance from the summit), (b) along the C–C' flow line from ~43 km to ~37 km, and (c)
27 along the D–D' flow line from ~41 km to ~32 km considering a time period of 500 years and
28 assuming time-independent surface mass balance. Ice flow velocities in the ice streams decrease
29 with time and this trend results in the overall decline of the outgoing ice flux. **Generally, the**
30 **modeled evolution is in agreement with observations of deglaciation of Severnaya Zemlya**
31 **archipelago.**

32

33 **1. Introduction**

34 There are relevant diagnostic observations of glaciers such as digital Landsat imagery and
35 satellite synthetic aperture radar interferometry (InSAR), airborne measurements, borehole ice
36 temperature and ice surface mass balance measurements. These observations provide data for
37 prognostic experiments that allow prediction of future glacier conditions for different climatic
38 scenarios in the future. These experiments can be performed employing the mathematical
39 modeling and in this study a two-dimensional ice flow model is applied for prediction of the
40 future conditions of fast-flowing ice streams on the southern side of the Academy of Sciences Ice
41 Cap in the Komsomolets Island, Severnaya Zemlya archipelago (Figure 1; Dowdeswell et al.,
42 2002).

43 The observations were based on digital Landsat imagery and satellite synthetic aperture radar
44 interferometry (InSAR) and revealed four drainage basins and four fast-flowing ice streams on
45 the southern side of the Academy of Sciences Ice Cap in the Komsomolets Island, Severnaya
46 Zemlya archipelago (Figure 2; Dowdeswell et al., 2002). The four ice streams are 17–37 km long
47 and 4–8 km wide (Dowdeswell et al., 2002). Bedrock elevations of these areas are below the sea
48 level, and the ice flow velocities attain a value of **70–140** m/a (Figure 2). Such fast flow-line

49 features are typical for outlet glaciers and ice streams in both the Arctic and the Antarctic. These
50 ice streams are the major locations of iceberg calving from the Academy of Sciences Ice Cap
51 (Dowdeswell et al., 2002).

52 The flow-line profiles of the three ice streams on the southern side of the Academy of Sciences
53 Ice Cap are shown in Figure 3. Ice flow in these ice streams is simulated with a two-dimensional
54 flow-line **higher-order** finite-difference model (e.g., Colinge and Blatter, 1998; Pattyn, 2000,
55 2002). This model describes an ice flow along a flow line (Pattyn, 2000, 2002). The results of the
56 diagnostic experiments obtained in (Konovalov, 2012), for instance, for the C–C' flow-line
57 profile show that the ice surface velocity along the flow line attains a value of 100 m/a assuming
58 that ice is sliding. However, the observed surface velocity distribution along the C–C' flow-line
59 profile (Dowdeswell et al., 2002) is not similar to that obtained by the model experiments for
60 constant values of friction coefficient and for both linear and nonlinear friction laws (Konovalov,
61 2012). Similarly, the diagnostic experiments carried out for the B–B' and D–D' profile data show
62 the same results for the ice flow velocities. The deviation between the observed and modeled
63 surface velocities suggests that the friction coefficient should be a spatially variable parameter.
64 Therefore, to achieve a better agreement between the observed and simulated velocities, the
65 spatial distribution of the friction coefficients requires to be optimized and an inverse problem
66 needs to be solved (e.g., MacAyeal, 1992; Sergienko et al., 2008; Arthern and Gudmundsson,
67 2010; Gagliardini et al., 2010; Habermann et al., 2010; Morlighem et al., 2010; Jay-Allemand et
68 al., 2011; Larour et al., 2012; **Sergienko and Hindmarsh, 2013**).

69 The inversion of friction coefficients is based on the minimization of the deviation between the
70 observed and modeled surface velocities. A series of test experiments (Konovalov, 2012), in
71 which modeled surface velocities are used as observations in the inverse problem, have shown
72 that the inverse problem for the full 2D ice flow-line model is ill posed. More precisely, the

73 surface velocity is weakly sensitive to small perturbations in friction coefficients, and as a result
74 the perturbations appear in the inverted friction coefficients (Konovalov, 2012).

75 Herein, in the prognostic experiments we use the friction coefficients inversions obtained by
76 applying the Tikhonov's regularization method, in which Tikhonov's stabilizing functional is
77 added to the main discrepancy functional (Tikhonov and Arsenin, 1977).

78 The inversions of friction coefficient are used in the prognostic experiments for the fast-flowing
79 ice streams. The considered 2D prognostic experiments are the numerical simulations with the ice
80 thickness distribution changes performed by the 2D flow-line thermo-coupled model, which
81 includes diagnostic equations as the heat-transfer equation and the mass-balance equation
82 (Pattyn, 2000, 2002). In this study, we present the results of the prognostic experiments
83 performed for the B–B', C–C', and D–D' profiles (Figure 3). Specifically, the prognostic
84 experiments are carried out for the three ice streams (Figure 2) that are the main sources of the
85 ice flux from the ice cap to the ocean. The results of the prognostic experiments include future
86 modeled histories of ice thickness distributions along the flow lines of grounding line locations
87 and outgoing ice fluxes. The surface mass balance in the performed experiments is considered as
88 time-independent, so the prognostic experiments show the assessment of the minimal ice mass
89 loss in the ice streams in the future, because the obtained forecasts don't include for future global
90 warming. Nevertheless, the results of the prognostic experiments are in agreement with the
91 observations of ice mass loss on the Severnaya Zemlya archipelago (Moholdt et al., 2012).

92

93 **2. Field equations**

94

95 **2.1. Forward problem: Diagnostic equations**

96

97 The 2D flow-line **higher-order** model includes the continuity equation for incompressible
 98 medium, the mechanical equilibrium equation in terms of stress deviator components (Pattyn,
 99 2000, 2002), and the rheological Glen law (Cuffey and Paterson, 2010):

100

$$\begin{cases}
 \int_{h_b}^z \frac{\partial u}{\partial x} dz' + \frac{1}{b} \frac{db}{dx} \int_{h_b}^z u dz' + w - w_b = 0, \\
 2 \frac{\partial \sigma'_{xx}}{\partial x} + \frac{\partial \sigma'_{yy}}{\partial x} + \frac{\partial^2}{\partial x^2} \int_z^{h_s} \sigma'_{xz} dz + \frac{\partial \sigma'_{xz}}{\partial z} = \rho g \frac{\partial h_s}{\partial x}, \\
 \sigma'_{ik} = 2\eta \dot{\epsilon}_{ik}; \quad \eta = \frac{1}{2} (mA(T))^{-\frac{1}{n}} \dot{\epsilon}^{\frac{1-n}{n}}, \\
 0 < x < L; \quad h_b(x) < z < h_s(x),
 \end{cases} \quad (1)$$

102

103 where (x,z) is a rectangular coordinate system with the x -axis along the flow line and the z -axis
 104 pointing vertically upward; u, w are the horizontal and vertical ice flow velocities, respectively; b
 105 is the width along the flow-line, σ'_{ik} is the stress deviator; $\dot{\epsilon}_{ik}$ is the strain-rate tensor; $\dot{\epsilon}$ is the
 106 second invariant of the strain-rate tensor; ρ is the ice density; g is the gravitational acceleration;
 107 η is the ice effective viscosity; $A(T)$ is the flow-law rate factor; T is the ice temperature; $h_b(x),$
 108 $h_s(x)$ are the ice bed and ice surface elevations, respectively; and L is the glacier length.

109 The boundary conditions and some complementary experiments that were carried out applying
 110 this model, were considered in (Konovalov, 2012). **In particular, the technique, when the**
 111 **boundary conditions are included in the momentum equations (Konovalov, 2012), was applied in**
 112 **the considered here prognostic experiments.**

113

114 **2.2. Inverse problem for the friction coefficient**

115

116 The inversion of friction coefficient has been carried out using the gradient minimization
117 procedure for the “smoothing” functional (Tikhonov and Arsenin, 1977):

118

$$119 \quad F = \int_0^L (u_{\text{obs}} - u_{\text{mod}})^2 dx + \beta \int_0^L \left(K_{\text{fr}}^2 + q(x) \left(\frac{d K_{\text{fr}}}{d x} \right)^2 \right) dx, \quad (2)$$

120

121 where u_{obs} are the observed velocities along the flow line and u_{mod} are the modeled velocities, the
122 first integral Φ is the discrepancy and the second integral Ω is the stabilizer (Tikhonov and
123 Arsenin, 1977), β is the regularization parameter, and $q(x)$ is considered equal to 1. The nonzero
124 value of β implies that the inverse problem, i.e., the problem that is based on the minimization of
125 the discrepancy Φ , is ill posed and the original problem of the discrepancy minimization is
126 replaced with the problem of the smoothing functional minimization.

127 The details of the gradient minimization procedure and the problem of the regularization
128 parameter choice are discussed in (Nagornov et al., 2006; Konovalov, 2012). In this manuscript
129 the inversions have been obtained for the linear (viscous) friction law, implying the experiments
130 implemented in (Konovalov, 2012) with the inversions for the C-C’ profile, that have shown a
131 good agreement between the observed (u_{obs}) and the calculated (u_{mod}) surface velocities for the
132 linear friction law.

133

134 **2.3. Prognostic equations**

135

136 The thermo-coupled prognostic experiments imply that the 2D flow-line model includes the heat-
137 transfer equation (Pattyn, 2000, 2002):

138

139
$$\frac{\partial T}{\partial t} = \chi \left(\frac{\partial^2 T}{\partial x^2} + \frac{1}{b} \frac{db}{dx} \frac{\partial T}{\partial x} + \frac{\partial^2 T}{\partial z^2} \right) - \left(u \frac{\partial T}{\partial x} + w \frac{\partial T}{\partial z} \right) + \frac{2A \frac{1}{n} \dot{\epsilon}^{\frac{1+n}{n}}}{\rho C}, \quad (3)$$

140

141 where χ and C are the thermal diffusivity and the specific heat capacity, respectively. **The**
 142 **terms in the first and in the second brackets respectively define the heat transfer due to heat**
 143 **diffusion and due to ice advection. The last term is associated with strain heating.**

144

145 In this model it is suggested that the ice surface temperature at the Academy of Sciences Ice Cap
 146 varies with an elevational gradient of temperature changes, which is equal to about $6.5 \text{ }^\circ\text{C}/\text{km}$.
 147 Hence, the ice surface temperature distribution along the flow line is defined by the temperature
 148 history at the summit $T_{s0}(t)$ and by the elevational changes, and it is expressed as

149
$$T_s(x,t) = T_{s0}(t) + \theta_T (h_s(0) - h_s(x)), \quad (4)$$

150 where θ_T is the elevational gradient. Therefore, Equation (4) provides the boundary condition on
 151 the ice surface. **However, it should be noted that Eq. (4) does not account firn warming through**
 152 **refreezing meltwater.**

153 The boundary condition at the ice base is defined by the geothermal heat flux and by the heating
 154 due to the basal friction, and it is expressed as (Pattyn, 2000, 2002)

155
$$\frac{\partial T}{\partial z} = -\frac{1}{k} (Q + (\sigma'_{xz})_b u_b), \quad (5)$$

156 where k is the thermal conductivity.

157 The boundary conditions at the ice (ice-shelf) terminus and at the ice-shelf base are defined by
 158 sea water temperature, which is considered as -2°C in this study.

159

160 The ice thickness temporal changes along the flow line are described by the mass-balance
161 equation (Pattyn, 2000, 2002):

162

$$163 \quad \frac{\partial H}{\partial t} = M_s - M_b - \frac{1}{b} \frac{\partial (\bar{u} b H)}{\partial x}, \quad (6)$$

164

165 where \bar{u} is the depth-averaged horizontal velocity, M_s is the annual surface mass balance, and
166 M_b is the melting rate at the ice base.

167 The mass-balance equation requires two boundary conditions at the summit and at the ice
168 terminus. The first condition at the ice cap summit implies that $\frac{\partial h_s}{\partial x} = 0$. The second condition

169 applied in the ice terminus originates from the fact that the ice thicknesses in the ice shelf along
170 the flow line attain a constant value at the terminus.

171

172 **2.3. Grounding line evolution**

173

174 In the model the grounding line position is defined from the hydrostatic equilibrium (Schoof,
175 2007; Pattyn et al., 2012; Seroussi et al., 2014). That is, since sea water flow under ice shelf is not
176 considered in the model and, hence, the pressure in Eq. (10)-(11) from Pattyn et al. (2012) is
177 equal to hydrostatic pressure, the grounding line position is at the location where

$$178 \quad -\rho_w h_r = H \rho \quad (7)$$

179 and h_r is the bedrock elevation, ρ_w is the water density.

180

181 3. Results of the numerical experiments

182

183 3.1 Inversions for the friction coefficient

184

185 For the first run of the friction coefficient inversions, the linear ice temperature profile
186 approximation is applied. Specifically, it is assumed that the ice temperature linearly increases
187 from -15°C at the surface to -5°C at the ice base at the division and increases from -2°C to
188 -1°C at the grounding line. Figure 4(a) shows the inverted friction coefficient distribution along
189 the C–C' flow line. The retrieved friction coefficient gradually decreases from $\sim 3.5 \times 10^3 \text{ Pa a}$
190 m^{-1} to a mean value of $5 \times 10^2 \text{ Pa a m}^{-1}$ within a distance of around $25 \text{ km} < x < 40 \text{ km}$ (Figure
191 4(a)). The difference between the simulated and *observed* surface velocities is relatively small
192 (Figure 4(b)) (Kononov, 2012).

193 The inverted friction coefficient distributions along the B–B' and D–D' flow lines show
194 qualitatively the same trends, i.e., they gradually decrease along the flow line from a high to a
195 lower level.

196 After the first run of the inversions, the ice temperature simulations are performed for inverted
197 friction coefficients and boundary conditions (4) and (5). Boundary condition (4) includes the
198 temperature history $T_{s0}(t)$. In particular, if the history is the past temperature (Nagornov et al.,
199 2005, 2006), which was inverted previously from the borehole temperature profile derived at the
200 **summit** of the Academy of Sciences Ice Cap (Zagorodnov, 1988; Arkhipov, 1999), **i.e. the**
201 **temperature history over the past 1000 years to present day (Nagornov et al., 2005, 2006)**, - then
202 we would expect the simulated output temperature close to the real present temperature in the ice
203 stream along the flow line. In other words, the modeled temperature will be close to the present
204 temperature (in the year when borehole measurements were performed), assuming a good

205 agreement between the model results and the real physical processes that occur in the glacier,
206 which are in general described by the model. The past surface temperature history, which was
207 applied in the simulations of the present ice temperature, was adopted from Nagornov et al.
208 (2005, 2006). The modeled present temperature distributions along the B–B', C–C' and D–D'
209 cross-sections are shown in Figure 5.

210 For the second run of the basal friction coefficient inversions, the modeled temperature
211 distributions are applied (the modeled temperature is defined from Eq. (3)..(5)). The inverted
212 friction coefficients (i) for the linearly approximated ice temperature and (ii) for the modeled ice
213 temperature are shown in Figure 6. Generally, the distinctions in the friction coefficients are
214 insignificant, and, therefore, the ice temperature approximations can be applied in the inverse
215 problem as the first iteration of the ice temperature distribution in the glacier.

216

217 **3.2. Prognostic experiments**

218

219 The main input data along with flow-line profiles for the prognostic experiments, namely, the
220 surface mass balance, are adopted from Bassford et al. (2006). Figure 7 shows the elevational
221 mass-balance distribution along the C–C' flow line, i.e., it shows how the surface mass balance
222 changes with elevation in the C–C' direction (Bassford et al., 2006). For the B–B' and D–D' flow
223 lines, the elevational mass-balance distributions are qualitatively the same (Bassford et al., 2006).

224 In the prognostic experiments that have been carried out, the mass balance is considered as time-
225 independent. That is, the elevational mass-balance distributions are kept unchanged for the
226 considered time period in the future. Thus, we intend to assess the maximum ice thickness in the
227 ice streams in the future, because the forecasts implemented with the time-independent surface
228 mass balance, don't imply a future global warming and, so, they don't suggest a future decreasing

229 of the surface mass balance M_s in Eq.(6). Similarly, the ice surface temperature is suggested to
230 be time-independent but dependent on elevation, i.e., according to Eq. (4), it is changed with
231 elevation with a constant value of $T_{s0}(t)$. From the borehole temperature measurements, the
232 present ice surface temperature at the summit is about -7.2°C . The initial ice temperatures
233 applied in the prognostic experiments are shown in Figure 5.

234 Despite that future warming scenarios are not included into the prognostic experiments, the
235 modeled ice cap response to the present environmental impact, which is reflected in the
236 elevational mass-balance distribution (Bassford et al., 2006), reveals that the ice thicknesses
237 gradually diminish along all the three flow lines. Figures 8(a)–10(a) show the modeled successive
238 ice surfaces divided into 50-year time intervals for the B–B', C–C', and D–D' profiles,
239 respectively. Figures 8(b)–10(b) show the same results as Figures 8(a)–10(a), respectively, but
240 these complementary figures show the evolutions of the three ice shelves in more detail. The
241 prognostic experiments are performed by applying a rectangular ice-shelf geometry. The
242 cumulative impact of sea water, surface mass balance, and ice flow changes in the glacier has
243 produced the future modeled ice shelf geometries. The ancillary black circles in Fig. 8(a,b)–
244 10(a,b) are aligned with the grid nodes and, thus, they show the spatial resolution, at which the
245 prognostic experiments have been implemented. The spatial resolution is irregular and it
246 decreases from about $2 \cdot 10^3$ m at the summit to about 10^2 m in the grounding line vicinity and in
247 the ice shelf. The spatial grid is considered unchangeable throughout the period of the modeling.

248 The grounding line history, i.e., grounding line retreat or advance, specifically reflects the
249 growing or diminishing ice mass, i.e., the history is an indicator of the glacier evolution. The
250 grounding line retreats (a) along the B–B' flow line from ~ 40 km to ~ 30 km (Fig. 11 (a)), (b)
251 along the C–C' flow line from ~ 43 km to ~ 37 km (Fig. 11 (b)), and (c) along the D–D' flow line
252 from ~ 41 km to ~ 32 km (Fig. 11 (c)) considering a time period of 500 years.

253 Furthermore, the results of the prognostic experiments can be likewise treated suggesting a
254 changes in the friction coefficient. The glacier terminus, currently fast flowing and therefore at
255 pressure melting, becomes eventually frozen to the ground – ice thickness insufficient to insulate
256 from cold atmosphere and reduced driving stress and strain heating. So basal friction
257 coefficients could change drastically, given the simulated changes in glacier geometry.

258 The ice flow velocities in the ice streams decrease with time and this trend diminishes the
259 outgoing ice fluxes in the future. Figure 12 shows the modeled outgoing ice flux histories, i.e., it
260 shows how the value $\bar{u} H b$, which is defined at the ice-shelf terminus, changes with time.

261 Accordingly, figure 13 shows the future history of the overall outgoing ice flux, i.e., it is the sum
262 of the three future modeled historical trends that are shown in Fig. 12.

263 There are small peaks that periodically disturb main historical trends of the three outgoing ice
264 fluxes. Every peak reflects ice calving at the ice-shelf terminus. Similarly, the ice calving
265 provides a sudden change in the value of the outgoing ice flux ($\bar{u} H b$) due to a sudden change in
266 the ice thickness (H) at the terminus. Considering a complex environmental impact on ice
267 shelves (Bassis et al., 2008), from the mathematical point of view it can be suggested that at long-
268 time scales the calving processes are described by a stochastic model, which considers the size of
269 the anticipated ice debris as a random value. This value satisfies a probability distribution law, for
270 instance, likewise the Gaussian distribution. In the model we considered the simplest probability
271 distribution, i.e. when the debris of equal length occur at each calving. Thus, the length of ice
272 debris is the parameter, which, in particular, corresponds the average length in a probability
273 distribution law (for instance, in the Gaussian distribution).

274 In this model the both ice-shelf length and ice-shelf thickness at the terminus are considered as
275 the variables that should satisfy a certain conditions. If the ice-shelf length exceeds a value l_{cr}

276 (the parameter of the model) or the ice-shelf thickness beside the terminus becomes smaller than
277 a value H_{cr} , then the calving of the appropriate part of ice occurs in the model.

278 To investigate the impact of the parameters on the results of the modeling, the parameters were
279 varied in a series of the experiments. However, the simulation reveals that at long-time scales the
280 mass balance, friction coefficient, ice temperature have the main impact to the assessment of the
281 grounding line retreat derived by the modeling.

282

283 **4. Discussion**

284

285 Numerical experiments carried out in the 2D model using the randomly perturbed friction
286 coefficient have revealed that the horizontal surface velocity is weakly sensitive to the
287 perturbations (Fig. 4 of Konovalov (2012)). Thus, the perturbations appear on the x -distributed
288 inverted friction coefficient. Therefore, the inverse problem should be considered as ill posed
289 because the weak sensitivity of the surface velocity to the perturbations in the friction coefficient
290 justifies the instability in the inverse problem. In other words, the instability in the inverse
291 problem means that small deviations in the observed surface velocities allow significant
292 perturbations in the friction coefficient. Hence, the application of the regularization method is
293 justified.

294 The Tikhonov's method that is based on the application of the stabilizing functional reduces the
295 effects of perturbations proportionally to the regularization parameter β (Tikhonov and Arsenin,
296 1977). A further increase in the parameter leads to a reduction in the real spatial variability of the
297 friction coefficients.

298 The reduction in the existent friction coefficient variability is associated with a growing
299 discrepancy between the observed and modeled surface velocities. Thus, the regularization

300 parameter is chosen as the value at which nonexistent perturbations are reduced, but the real
301 variability of the friction coefficient is not completely reduced by the stabilizing functional. The
302 optimal value of the regularization parameter can be defined approximately in the curve, which is
303 the deviation between the observed and modeled surface velocities versus the regularization
304 parameter (Leonov, 1994; Konovalov, 2012).

305 Evidently, the stabilizing functional narrows down the range of possible inverted x -distributions
306 of the friction coefficients. Thus, it is supposed *a priori* that the real **spatial distribution of the**
307 **friction coefficient with respect to the x -axis** is a smooth function. Moreover, the friction
308 coefficient in the friction laws is considered as a constant (e.g., Van der Veen, 1987; MacAyeal,
309 1989; Pattyn, 2000; Gudmundsson, 2011). Hence, the friction coefficient inversion performed for
310 the three cross-sections can be interpreted as follows.

311 **The two evidently distinguished levels in the inverted friction coefficient distributions can be**
312 **explained by changing the physical properties of the bedrock along the flow lines. Similarly, the**
313 **large values of the friction coefficient at $0 \text{ km} < x < 20 \text{ km}$ justify the rock-type bottom where ice**
314 **is frozen to the bed (the ice temperature at $0 \text{ km} < x < 20 \text{ km}$ is lower than the melting point). The**
315 **lower values of the friction coefficient at $25 \text{ km} < x < 40 \text{ km}$ presumably indicate the existence of**
316 **water-saturated till layer at the bottom (e.g., Engelhardt et al., 1978; Engelhardt et al., 1979;**
317 **Boulton, 1979; Boulton and Jones, 1979; MacAyeal, 1989; Engelhardt and Kamb, 1998; Iverson**
318 **et al., 1998; Tulaczyk et al., 2000). Specifically, the till layer (deformable basal sediments)**
319 **provides the basal ice sliding.**

320 The modeled present ice temperatures (Figure 5) are qualitatively the same in the three cross-
321 sections. There are resembling zones of relatively cold ice that can be distinguished in the
322 modeled temperatures approximately in the middle (**in vertical dimension**) of each cross-section.
323 These cold ice zones reflected the surface temperature minimum about 150–200 years ago in the
324 inverted past temperature history (Nagornov et al., 2005, 2006). This surface temperature

325 minimum corresponds to an event that is known as Little Ice Age. Thus, surface boundary
326 conditions (4), and diffusive and advective heat transfers provide the basal ice temperature that
327 mainly varies in the range -4 to -9°C at $25 \text{ km} < x < 40 \text{ km}$. Therefore, the modeled basal ice
328 temperature becomes lower than the melting point. Hence, the modeled ice temperatures justify
329 the sliding due to the existence of till layer at the bottom (Engelhardt et al., 1978; Engelhardt et
330 al., 1979; Boulton, 1979; Boulton and Jones, 1979; MacAyeal, 1989; Engelhardt and Kamb,
331 1998; Iverson et al., 1998; Tulaczyk et al., 2000).

332 However, note that the heat-transfer model considered here does not account for the melt water
333 refreezing in the subsurface firn layer (Paterson and Clarke, 1978). The numerical experiments
334 carried out in Paterson and Clarke (1978) have shown that the heat source demonstrated
335 significant impact due to melt water refreezing of the ice temperature profiles depending on the
336 melt water percolation depth. Thus, the notion that the basal ice temperature is higher than the
337 modeled temperature and could reach the melting point cannot be fully excluded.

338 General formulations of the friction laws assume that the appropriate equations include the
339 effective basal pressure (e.g., Budd et al., 1979; Iken, 1981; Bindschadler, 1983; Jansson, 1995;
340 Vieli et al., 2001; Pattyn, 2000). Introduction of the effective pressure in Equation (2) does not
341 provide a constant value of the inverted friction coefficient at $x > 25 \text{ km}$. The inversion
342 performed for the nonlinear Weertman-type friction law reveals similar variations in the inverted
343 friction coefficient at $x > 25 \text{ km}$ (Konovalov, 2012). The similar variability in the inverted
344 friction coefficients obtained for both the linear and nonlinear friction laws (Konovalov, 2012)
345 implies that the physical properties of the bedrock layer change according to the friction
346 coefficient distribution along the flow line. In particular, the presence of water in the bedrock
347 layer can be explained by the low bed elevations in the areas of fast-flowing ice streams (e.g.,
348 Knight, 1999; Vieli et al., 2001) or by a hydrological processes (e.g., Röthlisberger, 1972; Nye,
349 1976; Hewitt, 2011; Hoffman and Price, 2014). Therefore, the water content in the bedrock layer

350 can vary in agreement with the bed elevation changes, and the enhancement of water content at
351 lower elevations provides a decrease in the friction coefficient in the corresponding areas.

352 Finally, two areas can be distinguished in the **bedrock**, where basal ice is frozen to the bed (0 km
353 $< x < 20 \text{ km}$) and where there is basal sliding ($25 \text{ km} < x < 40 \text{ km}$) **due to the till layer**. The
354 boundary of transition from the area of the frozen basal ice to the area of the basal sliding is
355 diluted due to smoothing of the inverted friction coefficient by the stabilizer. The linear friction
356 law provides a good agreement between the observed and modeled surface velocity distributions
357 along the flow line. Thus, it can be conveniently applied in the applications (in particular, in the
358 prognostic experiments).

359 The prognostic experiments reveal that both ice mass and ice stream extents decline for the
360 reference time-independent mass balance (Bassford et al., 2006). These experiments demonstrate
361 that the grounding lines have retreated at about 10 km for the three ice streams considering a time
362 period of 500 years and a steady-state environmental impact, **which is meant a constant elevation-**
363 **dependent surface mass balance**. The ice flow velocities in the ice streams decrease with time due
364 to (a) diminishing of ice thicknesses (**and thus decreasing driving stress**) and (b) retreating of the
365 grounding lines from the sliding zones toward the zones where ice is frozen to the bed (inverted
366 friction coefficient distributions are considered as time-independent). Thus, the maxima of the ice
367 flow velocities in the ice streams decrease from $\sim 80\text{--}120 \text{ m/a}$ to $\sim 20\text{--}30 \text{ m/a}$. These trends in the
368 ice flow velocities diminish the outgoing ice fluxes (Fig. 12) and as a result diminish the overall
369 ice flux (Fig. 13).

370 **The observations in the Russian High Arctic (Moholdt et al., 2012) have revealed that over the**
371 **period between October 2003 and October 2009 the archipelagos have lost ice at a rate $-9.1 \pm$**
372 **2.0 Gt a^{-1} . Other this period the ice loss from Severnaya Zemlya is evaluated as $-1.4 \pm$**
373 **0.9 Gt a^{-1} (Moholdt et al., 2012). The modeling shows that other this period the Academy of**

374 Sciences Ice Cap (the largest of the ten glaciers located on Severnaya Zemlya) could lose about
375 0.2–0.3 $Gt a^{-1}$ (Fig. 13).

376

377 5. Conclusions

378

379 The modeled present ice temperatures (Figure 5) are qualitatively the same in the three cross-
380 sections. There are resembling zones of relatively cold ice that can be distinguished in the
381 modeled temperatures in the middle of the cross-sections. These cold ice zones reflected the
382 surface temperature minimum about 150–200 years ago in the inverted past temperature history
383 (Nagornov et al., 2005, 2006). This surface temperature minimum corresponds to an event that is
384 known as Little Ice Age.

385 The inversions of the friction coefficient performed for the three cross-sections can be interpreted
386 as follows. The two levels that are evidently distinguished in the inverted friction coefficient
387 distributions (Figure 6) can be explained by changing the physical properties of the bedrock
388 along the flow lines. Similarly, the large values of the friction coefficient at $0 \text{ km} < x < 20 \text{ km}$
389 justify the rock-type bottom where ice is frozen to the bed (the ice temperature at $0 \text{ km} < x < 20$
390 km is lower than the melting point). The lower values of the friction coefficient at $25 \text{ km} < x < 40$
391 km presumably indicate the existence of the till layer (or the sandy layer) at the bottom.
392 Specifically, the till layer provides the basal ice sliding.

393 The prognostic experiments carried out with the reference mass balance (Bassford et al., 2006)
394 show that the grounding line has been retreated at about 10 km in the three ice streams
395 considering a time period of 500 years. Similarly, the grounding line retreats (a) along the C–C'
396 flow line from ~43 km to ~37 km (the distance from the summit), (b) along the B–B' flow line
397 from ~40 km to ~30 km, and (c) along the D–D' flow line from ~41 km to ~32 km considering a

398 time period of 500 years and assuming time-independent mass balance. In the experiments, the
399 ice flow velocities in the ice streams decrease with time due to (a) diminishing of the ice
400 thicknesses and (b) retreating of the grounding lines from the sliding zones toward the zones
401 where ice is frozen to the bed. Thus, the maxima of the ice flow velocities in the ice streams
402 decrease from ~80–120 m/a to ~20–30 m/a. These trends in the ice flow velocities diminish the
403 outgoing ice fluxes and as a result diminish the overall ice flux (Figure 13). **The modeled
404 evolution of the ice streams is in agreement with observations of ice mass loss on Severnaya
405 Zemlya archipelago (Moholdt et al., 2012).**

406

407 **Acknowledgements.** The authors are grateful to Prof. J.A. Dowdeswell et al. for the data
408 that have been used in the manuscript. The authors are grateful to Prof. F. Pattyn for the useful
409 comments to the manuscript. The authors are grateful to Dr. T. Dunse and to the anonymous
410 referee for the reviewing the manuscript.

411

412 **References**

413

414 Arkhipov S.M.: Data Bank “Deep drilling of glaciers: Soviet-Russian Projects in Arctic, 1975–
415 1990”, Data of Glaciological Studies, 87, 229–238, 1999.

416 Arthern R. and H. Gudmundsson: Initialization of ice-sheet forecasts viewed as an inverse Robin
417 problem, *J. Glaciol*, 56, 527-533, 2010.

418 Bassford R.P., M.J. Siegert, J.A. Dowdeswell, J. Oerlemans, A.F. Glazovsky and Y.Y. Macheret:
419 Quantifying the Mass Balance of Ice Caps on Severnaya Zemlya, Russian High Arctic I: Climate
420 and Mass Balance of the Vavilov Ice Cap, *Arctic, Antarctic, and Alpine Research*, 38 (1), 1-12,
421 2006.

422 Bassis J.N., H.A. Fricker, R. Coleman, J.-B. Minster: An investigation into the forces that drive
423 ice-shelf rift propagation on the Amery Ice Shelf, East Antarctica, *J. Glaciol*, 54, 17-27, 2008.

424 Cuffey K. and W.S.B. Paterson: *The physics of glaciers*, 4th ed., Butterworth-Heineman,
425 Elsevier, 2010.

426 Bindschadler R.: The importance of pressurized subglacial water in separation and sliding at the
427 glacier bed, *J. Glaciol*, 29(101), 3-19, 1983.

428 Boulton G.S.: Processes of glacier erosion on different substrata, *J. Glaciol*, 23(89), 15-38, 1979.

429 Boulton G.S. and A.S. Jones: Stability of temperate ice caps and ice sheets resting on beds of
430 deformable sediment, *J. Glaciol*, 24(90), 29-43, 1979.

431 Budd W.E., P.L. Keage and N.A. Blundy: Empirical studies of ice sliding, *J. Glaciol*, 23(89),
432 157-170, 1979.

433 Colinge J., H. Blatter: Stress and velocity fields in glaciers: Part I. Finite difference schemes for
434 higher-order glacier models, *J. Glaciol*, 44, 448-456, 1998.

435 Dowdeswell J.A., R.P. Bassford, M.R. Gorman, M. Williams, A.F. Glazovsky, Y.Y. Macheret,
436 A.P. Shepherd, Y.V. Vasilenko, L.M. Savatyugin, H.W. Hubberten and H. Miller: Form and flow
437 of the Academy of Sciences Ice Cap, Severnaya Zemlya, Russian High Arctic. *J. Geophys Res*,
438 107, 1-15, 2002.

439 Engelhardt H.F., W.D. Harrison, and B. Kamb: Basal sliding and conditions at the glacier bed as
440 revealed by bore-hole photography, *J. Glaciol*, 20(84), 469-508, 1978.

441 Engelhardt, H.F., B. Kamb, C.F. Raymond, and W.D. Harrison: Observation of basal sliding of
442 Variegated Glacier, Alaska, *J. Glaciol*, 23(89), 406-407, 1979.

443 Engelhardt H. and B. Kamb: Basal sliding of Ice Stream B, West Antarctica, *J. Glaciol*, 44(147),
444 223-230, 1998.

445 Gagliardini O., M. Jay-Allemand, F. Gillet-Chaulet: Friction distribution at the base of a surging
446 glacier inferred from an inverse method, San Francisco, CA, USA, AGU Fall Meeting, 2010 Dec.
447 13-17, Abstract: C13A-0540.

448 Gudmundsson G.H.: Ice-stream response to ocean tides and the form of the basal sliding law, *The*
449 *Cryosphere*, 5, 259–270, 2011.

450 Habermann M., D.A. Maxwell, M. Truffer: A principled stopping criterion for the reconstruction
451 of basal properties in ice sheets. San Francisco, CA, USA, AGU Fall Meeting, 2010 Dec. 13-17,
452 Abstract: C21C-0556.

453 Hewitt I.J.: Modelling distributed and channelized subglacial drainage. The spacing of channels,
454 *J. Glaciol.*, 57(202), 302–314, doi:10.3189/002214311796405951, 2011.

455 Hoffman M. and S. Price: Feedbacks between coupled subglacial hydrology and glacier
456 dynamics, *J. Geophys. Res.: Earth Surf.*, 119, doi: 10.1002/2013JF002943, 2014.

457 Iken A.: The effect of the subglacial water pressure on the sliding velocity of a glacier in an
458 idealized numerical model, *J. Glaciol.*, 27(97), 407–421, 1981.

459 **Iverson N. R., T. S. Hooyer, R. W. Baker: Ring-shear studies of till deformation: Coulomb-**
460 **plastic behavior and distributed strain in glacier beds, *J. Glaciol.*, 44:634–642, 1998.**

461 Jansson P.: Water pressure and basal sliding on Storglaciären, northern Sweden, *J. Glaciol.*,
462 41(138), 232–240, 1995.

463 Jay-Allemand M., F. Gillet-Chaulet, O. Gagliardini, M. Nodet: Investigating changes in basal
464 conditions of Variegated Glacier prior to and during its 1982-1983 surge, *Cryosphere*, 5, 659-
465 672, 2011.

466 Knight P.G.: *Glaciers*, Stanley Thornes, Cheltenham, UK, 1999.

467 Konovalov Y.V.: Inversion for basal friction coefficients with a two-dimensional flow line model
468 using Tikhonov regularization, *Research in Geophysics*, 2:e11, 82-89, 2012.

469 Larour E., H. Seroussi, M. Morlighem, E. Rignot: Continental scale, high order, high spatial
470 resolution, ice sheet modeling using the Ice Sheet System Model (ISSM), *J Geophys Res*, 117, 1-
471 20, 2012.

472 Li X., Bo Sun, M.G. Siegert, R.G. Bingham, X. Tang, D. Zhang, X. Cui, X. Zhang:
473 Characterization of subglacial landscapes by a two-parameter roughness index, *J. Glaciol*,
474 56(199), 831–836, 2010.

475 Leonov A.S.: Some a posteriori termination rules for the iterative solution of linear ill-posed
476 problems. *Comput Math Math Phys*, 34, 121-126, 1994.

477 MacAyeal D.R.: Large-scale ice flow over a viscous basal sediment: theory and application to ice
478 stream B, Antarctica, *J Geophys Res*, 94, 4071–4088, 1989.

479 MacAyeal D.R.: The basal stress-distribution of Ice Stream-E, Antarctica, inferred by control
480 methods, *J Geophys Res, Solid Earth*, 97, 595-603, 1992.

481 **Moholdt, G., B. Wouters, A. S. Gardner: Recent mass changes of glaciers in the Russian High**
482 **Arctic, *Geophys. Res. Lett.*, 39, L10502, doi:10.1029/2012GL051466, 2012.**

483 Morlighem M., E. Rignot, H. Seroussi, E. Larour, H. Ben Dhia and D. Aubry: Spatial patterns of
484 basal drag inferred using control methods from a full-Stokes and simpler models for Pine Island
485 Glacier, West Antarctica, *Geophys Res Lett*, 37, L14502, doi:10.1029/2010GL043853, 2010.

486 Nagornov O.V., Y.V. Konovalov, V. Tchijov: Reconstruction of past temperatures for Arctic
487 glaciers subjected to intense subsurface melting, *Ann Glaciol*, 40, 61-66, 2005.

488 Nagornov O.V., Y.V. Konovalov, V. Tchijov: Temperature reconstruction for Arctic glaciers,
489 *Palaeogeogr Palaeoclimatol Palaeoecol*, 236, 125-134, 2006.

490 Nye J. F.: Water flow in glaciers: jökulhlaups, tunnels and veins, *J. Glaciol*, 17(76), 181–207,
491 1976.

492 Paterson W.S.B. and G.K.S. Clarke: Comparison of theoretical and observed temperatures
493 profiles in Devon Island ice cap, Canada, *Geophys. J. of R. Astron. Soc.*, 55(3), 615-632, 1978.

494 Pattyn F.: Ice-sheet modeling at different spatial resolutions: focus on the grounding zone, *Ann*
495 *Glaciol*, 31, 211-216, 2000.

496 Pattyn F.: Transient glacier response with a higher-order numerical ice-flow model, *J. Glaciol*,
497 48, 467-477, 2002.

498 Pattyn, F., C. Schoof, L. Perichon, R. C. A. Hindmarsh, E. Bueler, B. de Fleurian, G. Durand, O.
499 Gagliardini, R. Gladstone, D. Goldberg, G. H. Gudmundsson, P. Huybrechts, V. Lee, F. M. Nick,
500 A. J. Payne, D. Pollard, O. Rybak, F. Saito, and A. Vieli: Results of the Marine Ice Sheet Model
501 Intercomparison Project, *MISMIP, The Cryosphere*, 6(3):573–588, 2012.

502 Röthlisberger H.: Water pressure in intra- and subglacial channels, *J. Glaciol.*, 11(62), 77–203,
503 1972.

504 Sergienko O.V., R.A. Bindschadler, P.L. Vornberger, D.R. MacAyeal: Ice stream basal
505 conditions from block-wise surface data inversion and simple regression models of ice stream
506 flow: Application to Bindschadler Ice Stream, *J Geophys Res*, 113, 1-11, 2008.

507 Schoof, C.: Ice sheet grounding line dynamics: Steady states, stability, and hysteresis, *J.*
508 *Geophys. Res.*, 112, 1–19, doi:10.1029/2006JF000664, 2007.

509 Sergienko, O. V. and R. C. A. Hindmarsh: Regular patterns in frictional resistance of ice-stream
510 beds seen by surface data inversion, *Science*, 342(6162):1086–1089, 2013.

511 Seroussi, H., M. Morlighem, E. Larour, E. Rignot, A. Khazendar: Hydrostatic grounding line
512 parameterization in ice sheet models, *The Cryosphere*, 8, 2075–2087, 2014.

513 Tikhonov A.N., V.Ia. Arsenin: Solutions of ill posed problems, Washington: Winston & Sons,
514 1977.

515 Tulaczyk, S., W. B. Kamb, H. F. Engelhardt: Basal mechanics of Ice Stream B, West Antarctica
516 I. Till mechanics. *J. Geophys. Res.*, 105:463–482, doi:10.1029/1999JB900329, 2000.

517 Van der Veen C.J. Longitudinal stresses and basal sliding: a comparative study. In: Van der Veen
518 C.J., Oerlemans J., (eds). Dynamics of the West Antarctic ice sheet. Dordrecht: D. Reidel
519 Publishing Co., 223-248, 1987.

520 Vieli A., M. Funk, H. Blatter: Flow dynamics of tidewater glaciers: a numerical modelling
521 approach, *J. Glaciol.*, 47(159), 595–606, 2001.

522 Weertman J.: On the sliding of glaciers, *J. Glaciol.*, 3(21), 33–38, 1957.

523 Zagorodnov V.S.: Recent Soviet activities on ice core drilling and core investigations in Arctic
524 region. *Bulletin of Glacier Research, Data Center for Glacier Research, Japanese Society of*
525 *Snow and Ice*, 6, 81–84, 1988.

526



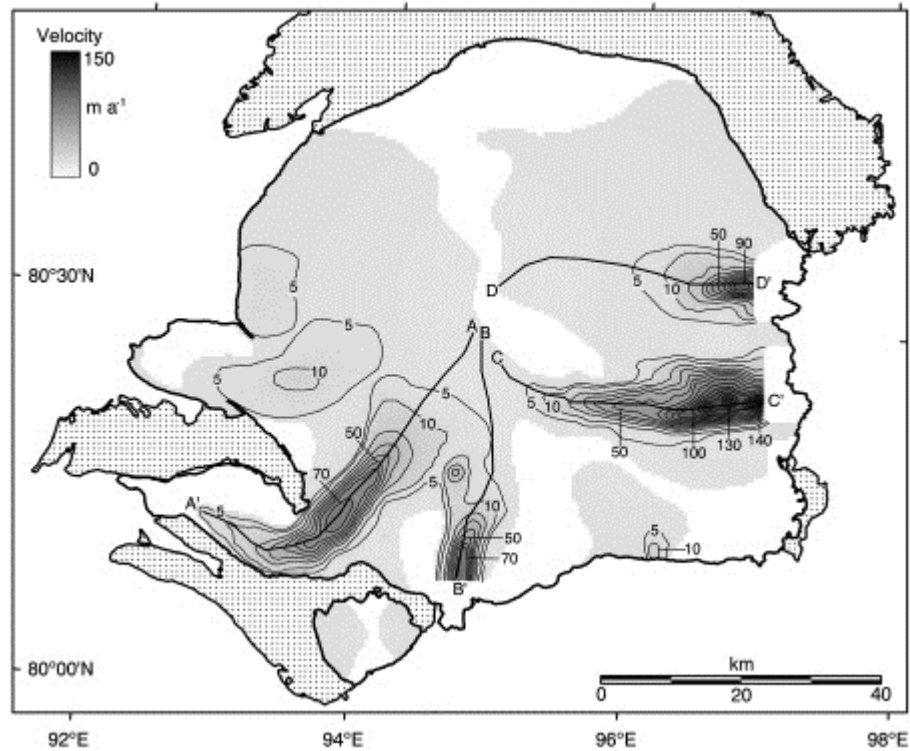
527

528

529

530 **Figure 1 (after Dowdeswell et al. (2002)).** Map of Severnaya Zemlya showing the Academy of
 531 Sciences Ice Cap on Komsomolets Island together with the other ice caps in the archipelago:
 532 Rusanov Ice Cap, Vavilov Ice Cap, Karpinsky Ice Cap, University Ice Cap, Pioneer Glacier,
 533 Semenov-Tyan Shansky Glacier, Kropotkin Glacier, Leningrad Glacier. Inset is the location of
 534 Severnaya Zemlya and the nearby Russian Arctic archipelagos of Franz Josef Land and Novaya
 535 Zemlya within the Eurasian High Arctic.

536



538

539

540

541 **Figure 2 (after Dowdeswell et al. (2002)).** Corrected interferometrically derived ice surface
 542 velocities for the Academy of Sciences Ice Cap. The first two contours are at velocities of 5 and
 543 10 m a^{-1} , with subsequent contours at 10 m a^{-1} intervals. The unshaded areas of the ice cap are
 544 regions of non-corrected velocity data. The dotted areas represent bare land. The four fast
 545 flowing ice stream central lines are denoted as A-A', B-B', C-C', D-D', respectively. Velocity
 546 profiles A-A' to D-D' are shown in Figure 11 of Dowdeswell et al. (2002)

547

548

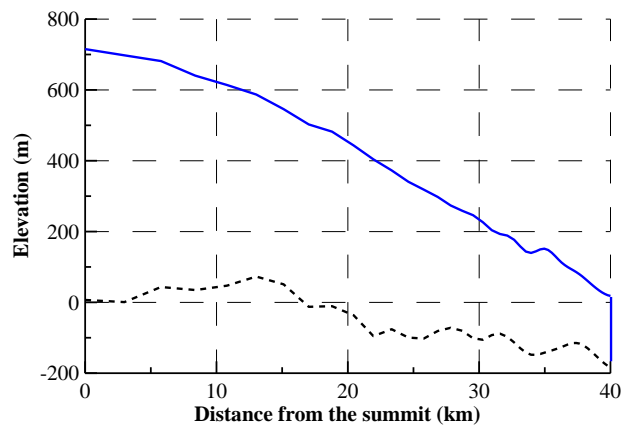


Fig. 3 (a)

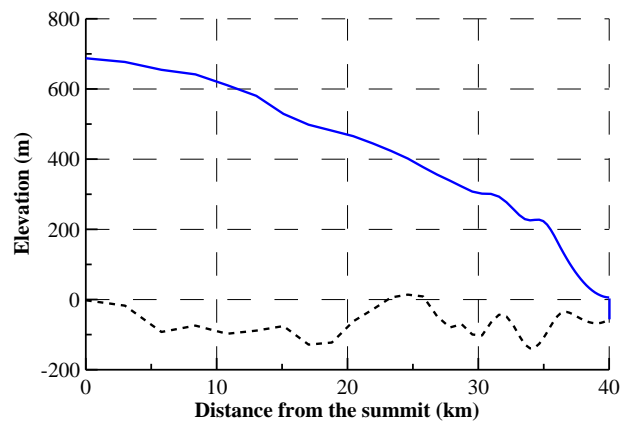


Fig. 3 (b)

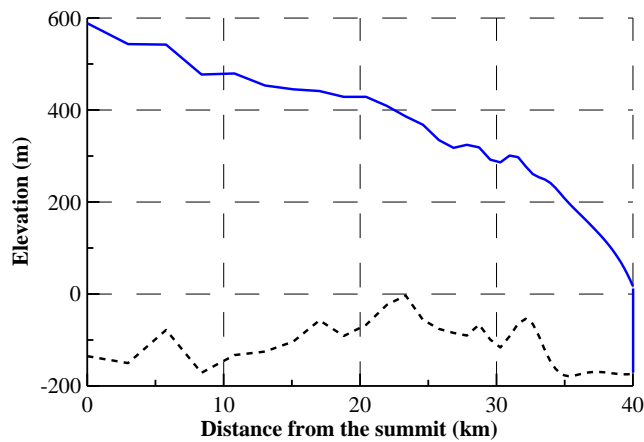
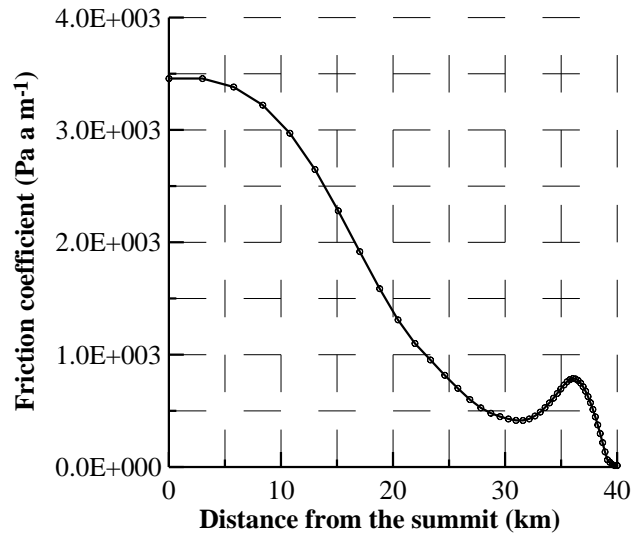


Fig. 3 (c)

Figure 3. (a) B-B' flow line profile, which crosses downstream one of the four fast flowing ice streams in the Academy of Sciences Ice Cap (Fig. 2). (b) C-C' flow line profile. (c) D-D' flow line profile. The data of ice surface and ice bed elevations are imported from Figure 8 of Dowdeswell et al. (2002).

561

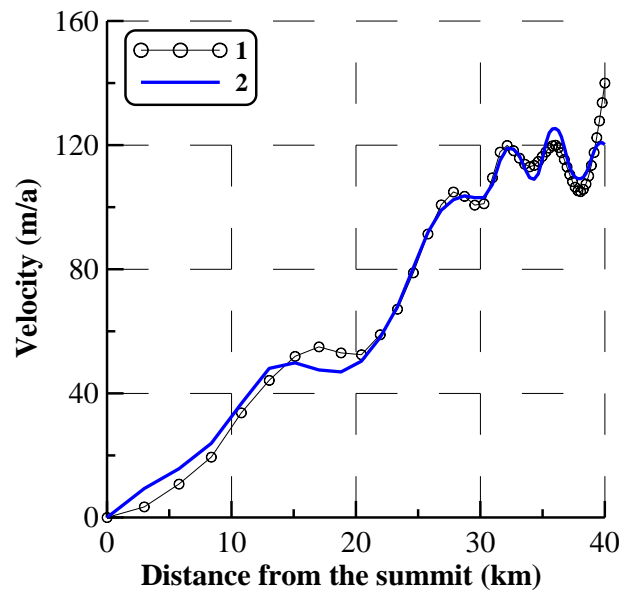


562

563

Fig. 4 (a)

564



565

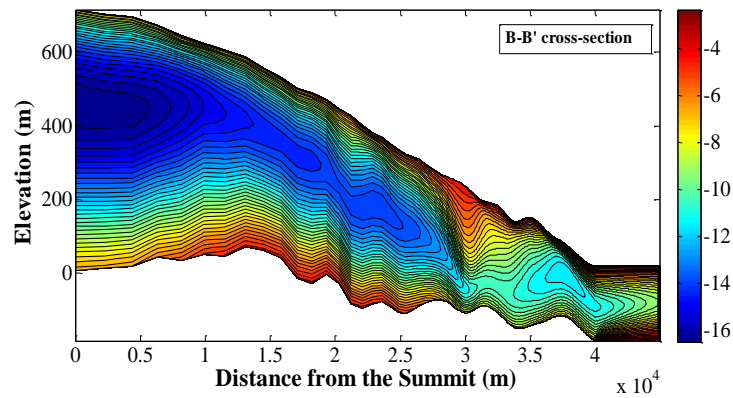
566

Fig. 4 (b)

567 **Figure 4. (a)** The friction coefficient distribution are obtained in the inverse problem for *the*
568 *linear friction law* and for the observed surface velocity distribution along the C-C' flow line. **(b)**
569 The ice surface horizontal velocity distributions along the flow line: **1** – the observed surface
570 velocity distribution, taken from Figure 11 of Dowdeswell et al. (2002), **2** - the modeled surface
571 velocity distribution, which corresponds to the reconstructed friction coefficient in Fig. 4,a.

572

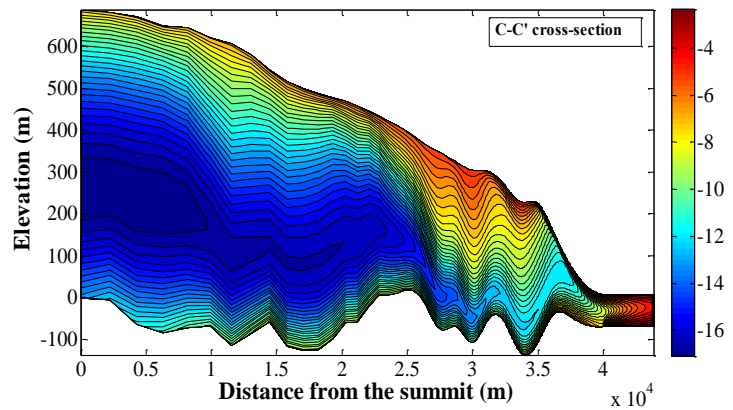
573



574

575

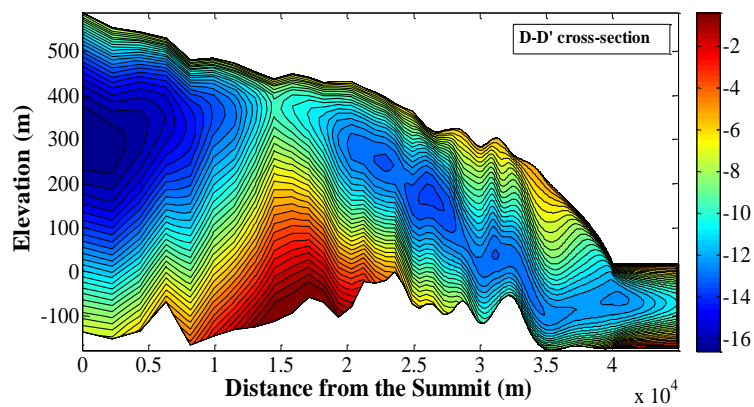
Fig. 5 (a)



576

577

Fig. 5 (b)



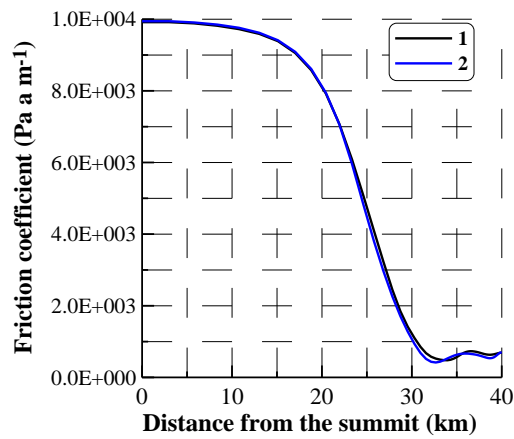
578

579

Fig. 5 (c)

580 **Figure 5.** The temperature distributions within (a) the B-B' cross-section, (b) C-C' cross-section
581 and (c) D-D' cross-section simulated by the model with the past surface temperature history based
582 on the paleo-temperature, which is retrieved from the borehole temperature data (Nagornov et al.,
583 2005, 2006).

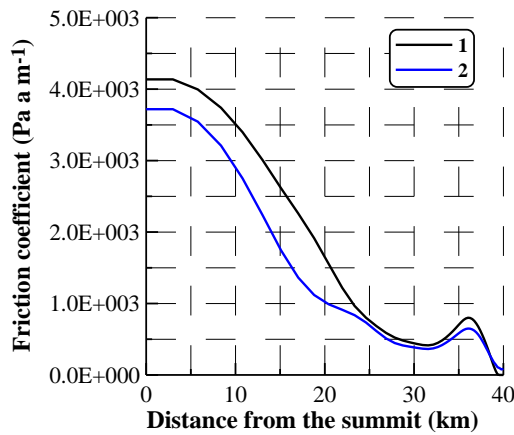
584



585

586

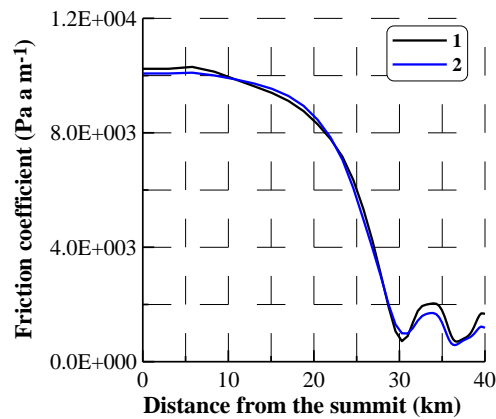
Fig. 6 (a)



587

588

Fig. 6 (b)



589

590

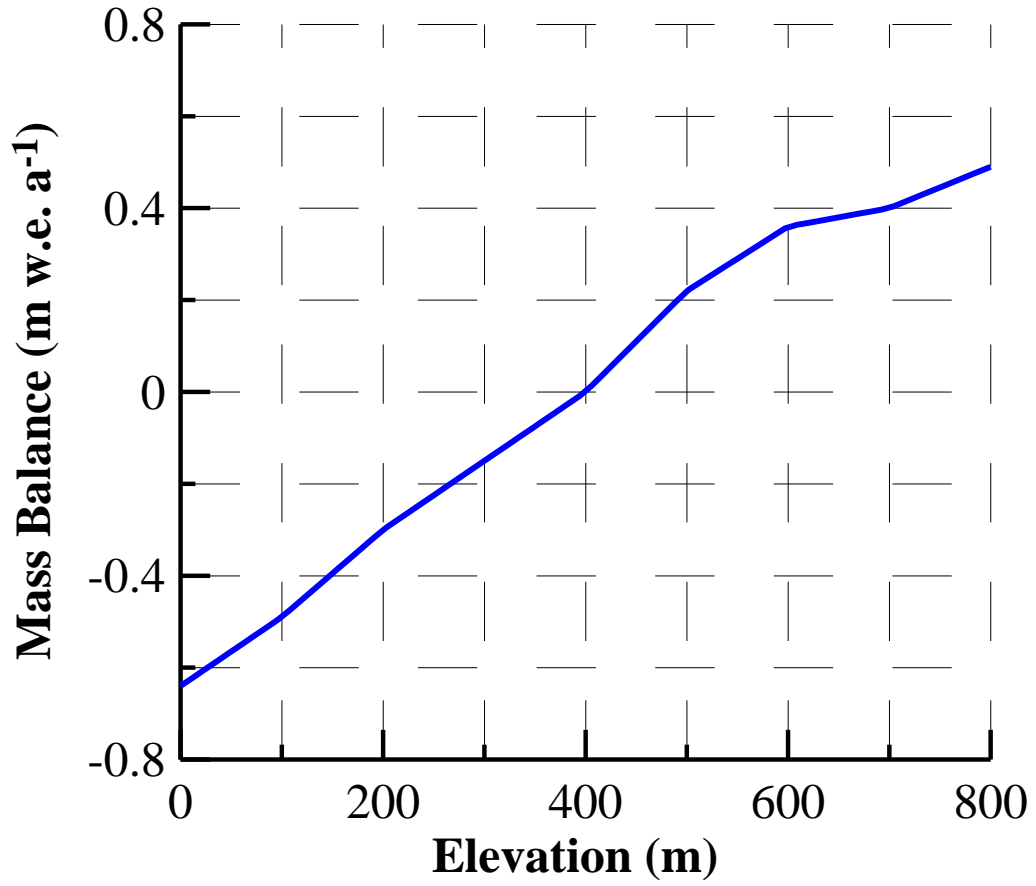
591

Fig. 6 (c)

592 **Figure 6.** The friction coefficients inverted along (a) B-B' flow line, (b) C-C' flow line and (c) D-
 593 D' flow line. Curve 1 is the first inversion, which is obtained for the linear ice temperature
 594 profiles (the ice temperature approximation for the initial inversions). Curve 2 is the second
 595 inversion, which corresponds to the modeled ice temperature (Fig. 5).

596

597
598
599
600



601
602
603
604
605
606

Figure 7. The surface mass balance elevational distribution along the C-C' flow line (Bassford et al., 2006).

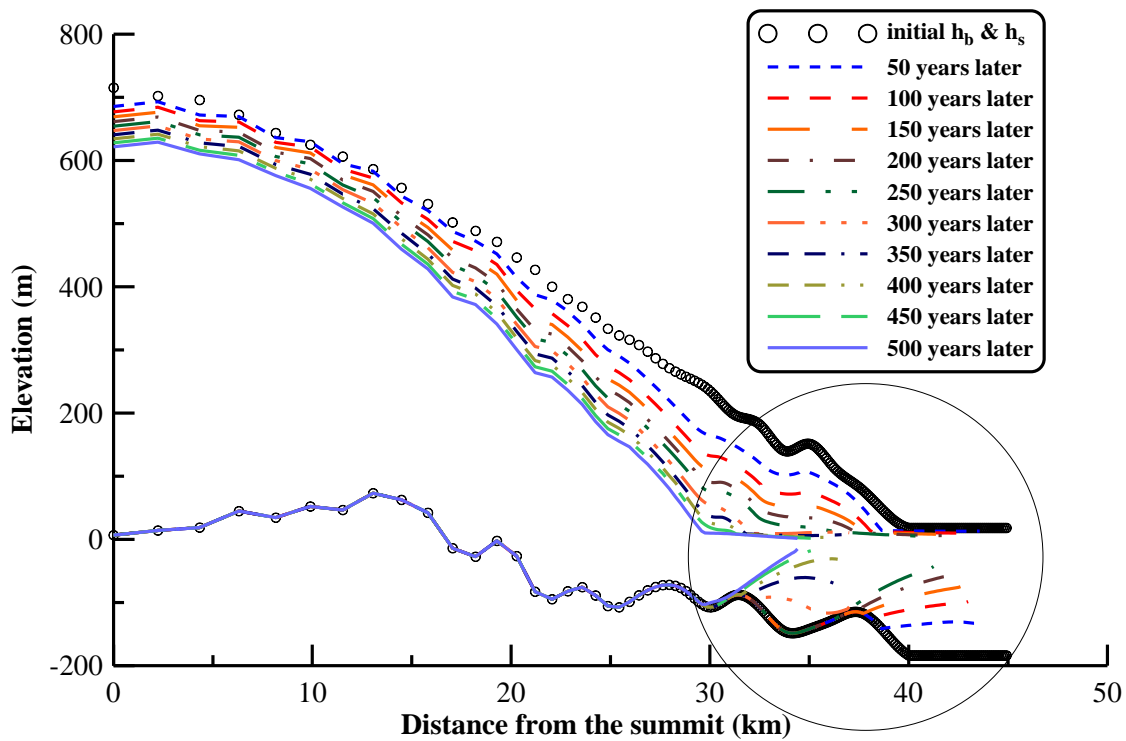


Fig. 8 (a)

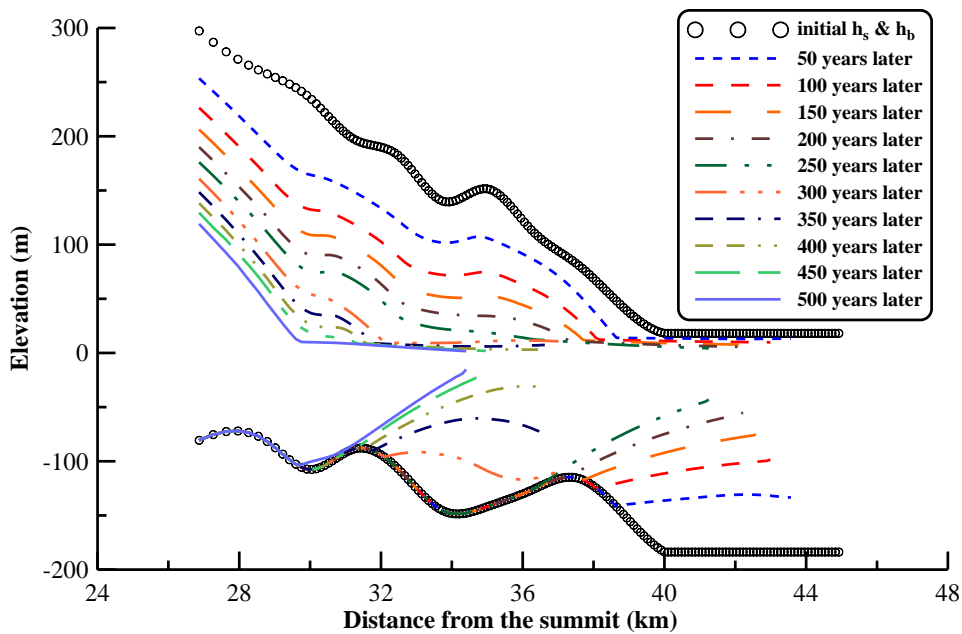


Fig. 8 (b)

Figure 8. (a) The modeled successive B-B' cross-section geometries separated by 50-year intervals from the present to the future 500 years later. (b) A magnified section of panel (a), showing the evolution of B-B' ice shelf.

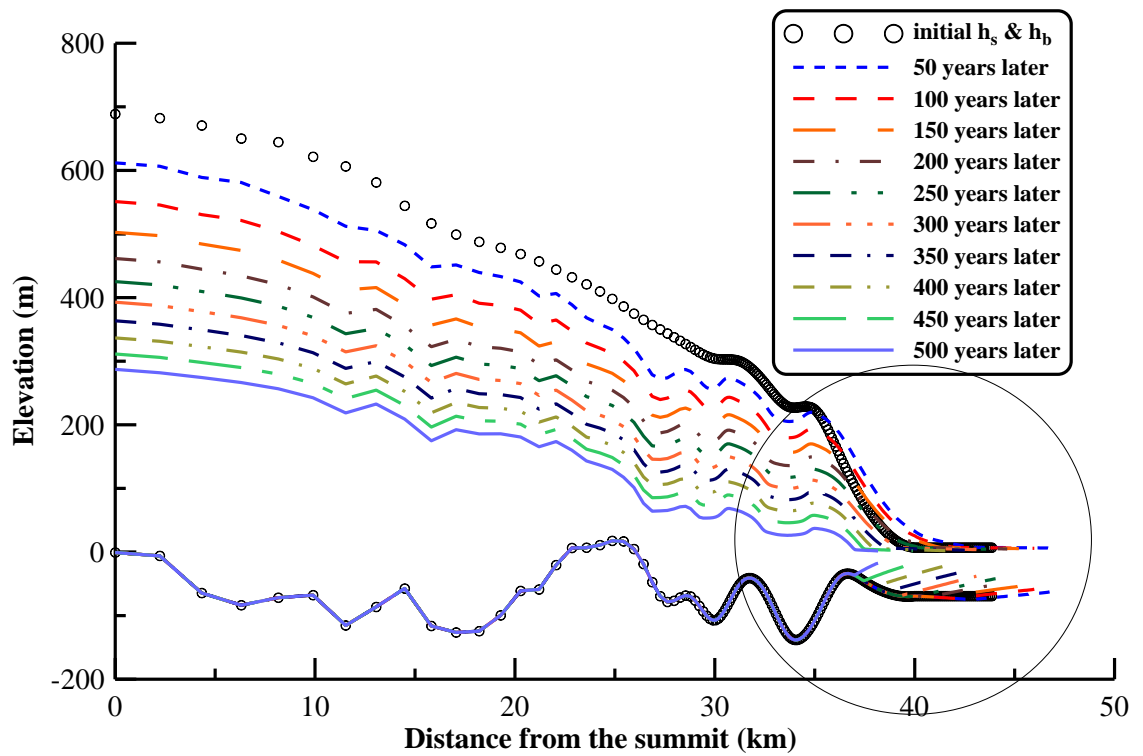


Fig. 9 (a)

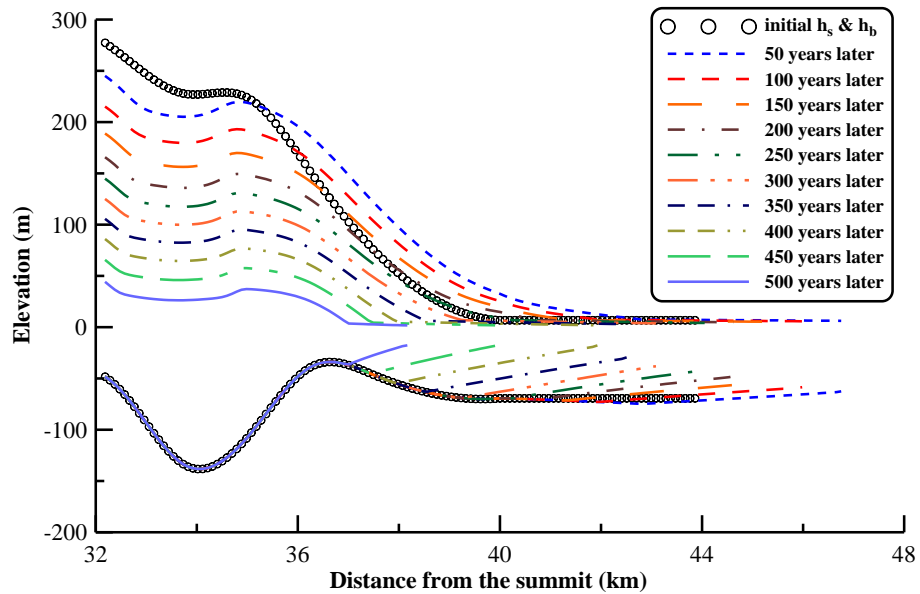


Fig. 9 (b)

Figure 9. (a) The modeled successive C-C' cross-section geometries separated by 50-year intervals from the present to the future 500 years later. (b) A magnified section of panel (a), showing the evolution of C-C' ice shelf.

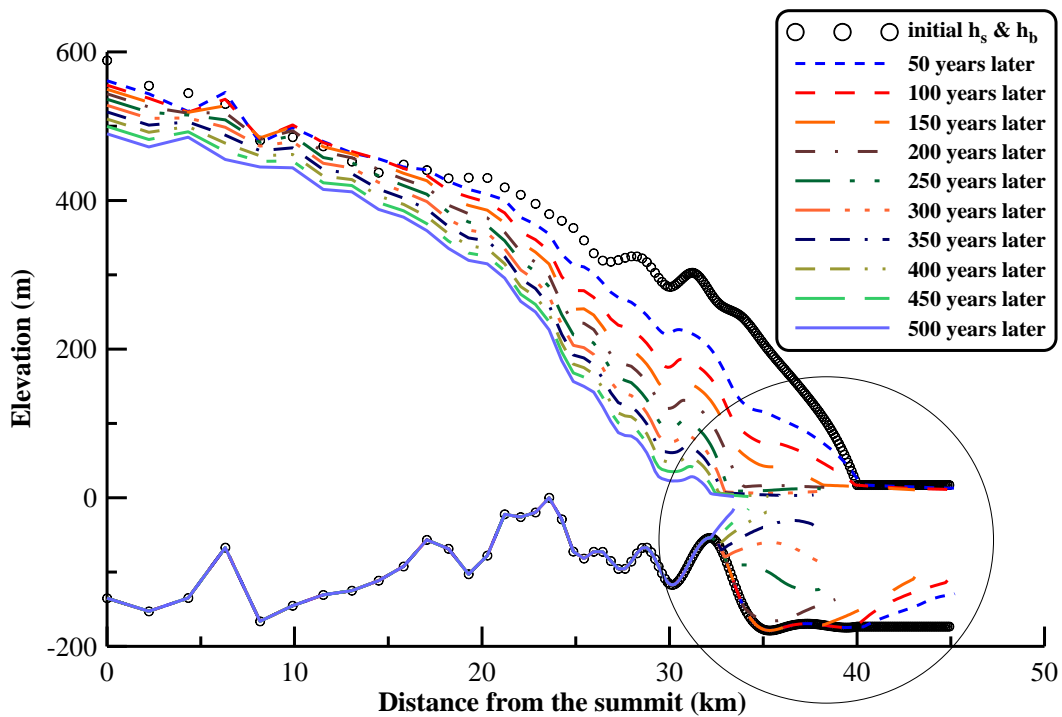


Fig. 10 (a)

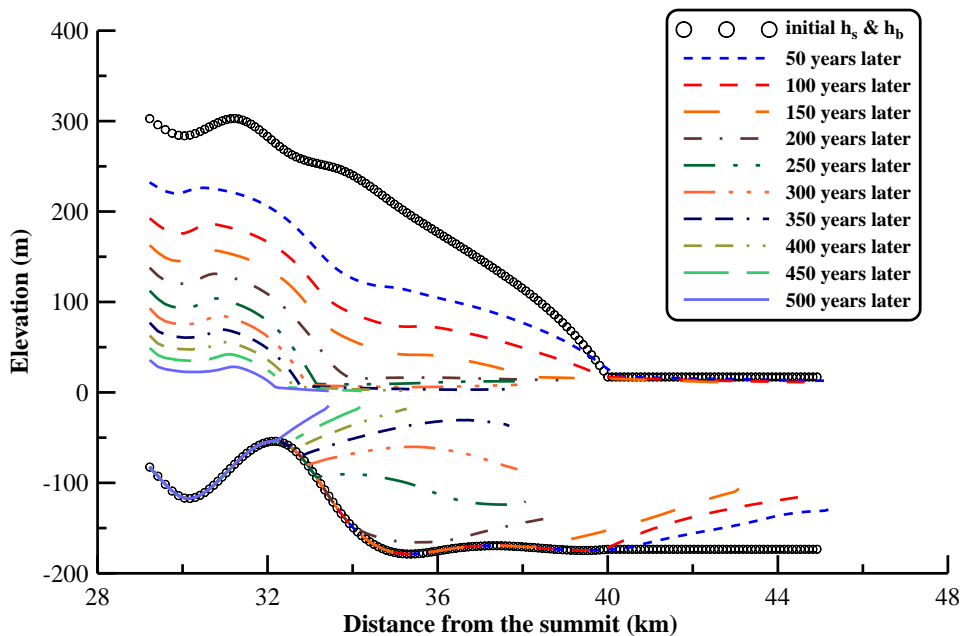
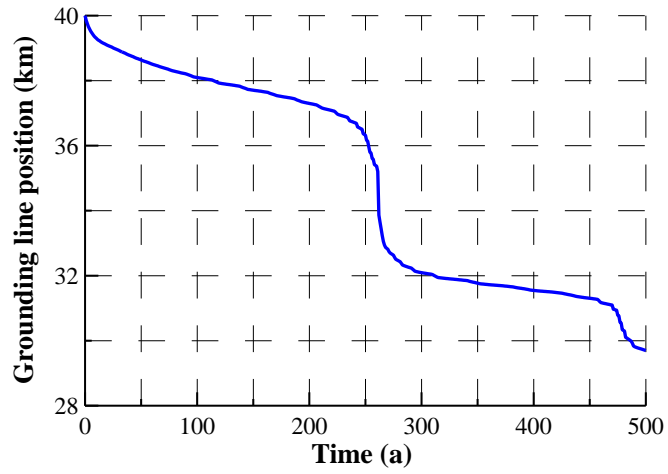


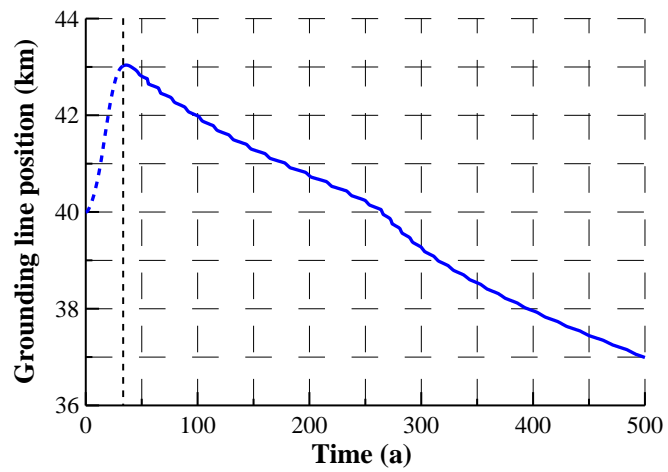
Fig. 10 (b)

Figure 10. (a) The modeled successive D-D' cross-section geometries separated by 50-year intervals from the present to the future 500 years later. (b) A magnified section of panel (a), showing the evolution of D-D' ice shelf.



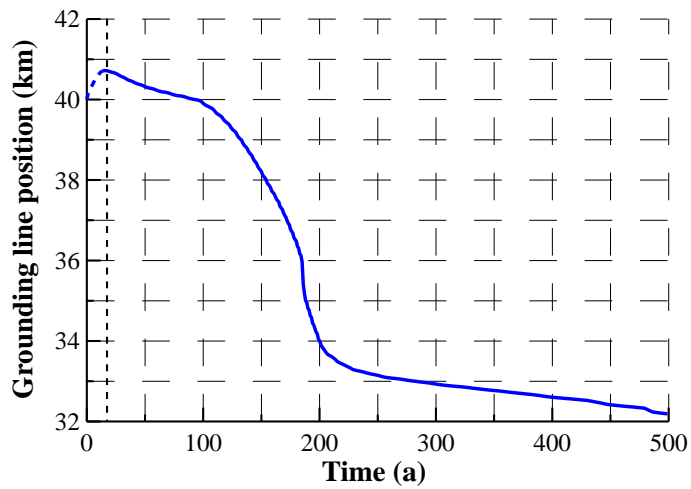
634
635

Fig. 11 (a)



636
637

Fig. 11 (b)

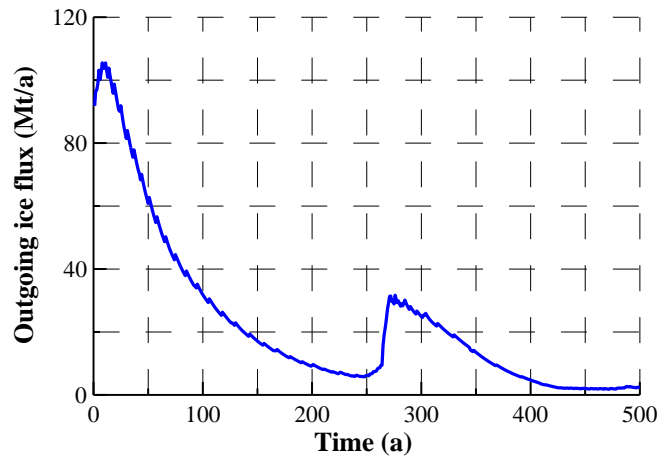


638
639
640

Fig. 11 (c)

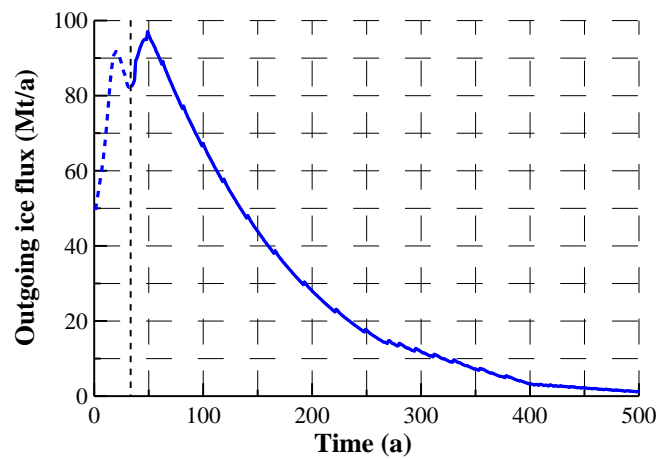
641 **Figure 11.** The modeled grounding line history (a) for B-B' cross section (b) for C-C' and (c) for
642 D-D' cross section.

643



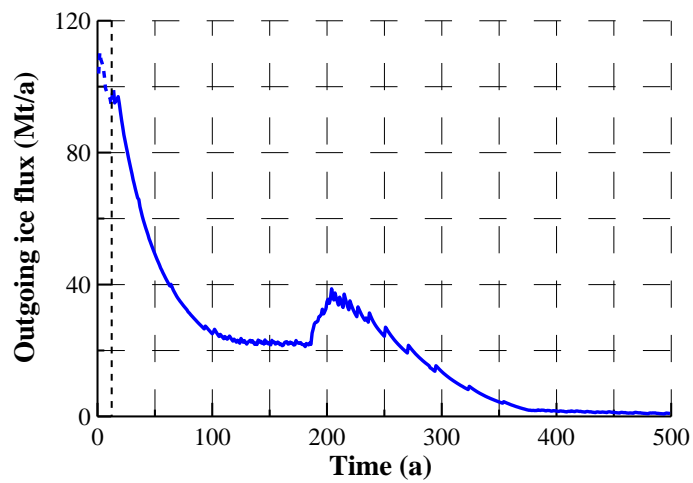
644
645

Fig. 12 (a)



646
647

Fig. 12 (b)

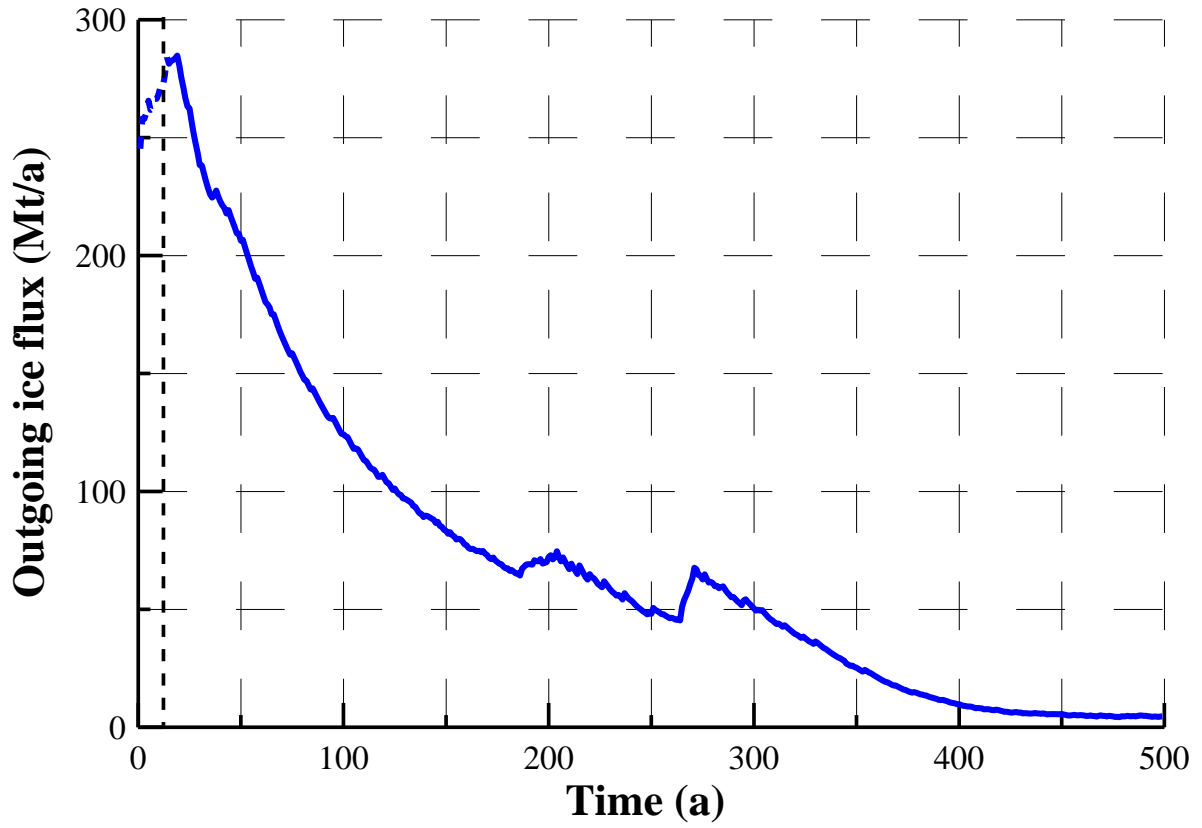


648
649
650

Fig. 12 (c)

651 **Figure 12.** The modeled outgoing ice flux history (a) for B-B' cross section (b) for C-C' and (c)
652 for D-D' cross section.
653

654
655
656
657



658
659
660
661
662
663
664

Figure 13. The overall outgoing ice flux history (the sum of the outgoing fluxes for the three ice streams: B-B', C-C' and D-D').